

Depth of interaction decoding of a continuous crystal detector module

T Ling¹, T K Lewellen² and R S Miyaoka²

¹ Department of Physics, University of Washington, Seattle, WA 98107, USA

² Department of Radiology, University of Washington, Seattle, WA 98107, USA

E-mail: lingtop@u.washington.edu

Received 23 November 2006, in final form 13 February 2007

Published 29 March 2007

Online at stacks.iop.org/PMB/52/2213

Abstract

We present a clustering method to extract the depth of interaction (DOI) information from an 8 mm thick crystal version of our continuous miniature crystal element (cMiCE) small animal PET detector. This clustering method, based on the maximum-likelihood (ML) method, can effectively build look-up tables (LUT) for different DOI regions. Combined with our statistics-based positioning (SBP) method, which uses a LUT searching algorithm based on the ML method and two-dimensional mean–variance LUTs of light responses from each photomultiplier channel with respect to different gamma ray interaction positions, the position of interaction and DOI can be estimated simultaneously. Data simulated using DETECT2000 were used to help validate our approach. An experiment using our cMiCE detector was designed to evaluate the performance. Two and four DOI region clustering were applied to the simulated data. Two DOI regions were used for the experimental data. The *misclassification rate* for simulated data is about 3.5% for two DOI regions and 10.2% for four DOI regions. For the experimental data, the rate is estimated to be ~25%. By using multi-DOI LUTs, we also observed improvement of the detector spatial resolution, especially for the corner region of the crystal. These results show that our ML clustering method is a consistent and reliable way to characterize DOI in a continuous crystal detector without requiring any modifications to the crystal or detector front end electronics. The ability to characterize the depth-dependent light response function from measured data is a major step forward in developing practical detectors with DOI positioning capability.

1. Introduction

While there have been numerous techniques proposed to extract depth of interaction (DOI) information from discrete crystal detectors (Moses *et al* 1993, Miyaoka *et al* 1998, Seidel

et al 1998, Yamamoto and Ishibashi 1998, Saoudi *et al* 1999, Shao *et al* 2002, Burr *et al* 2004), there have been a limited number of methods proposed to extract DOI information from continuous crystal detectors for PET imaging (LeBlanc *et al* 2004, Tavernier *et al* 2005, Lerche *et al* 2005). The main techniques have been to model the light distribution in the detector through computer simulation and use these results to estimate DOI from the collected light signals. The chief limitation of this approach is that it is extremely difficult to accurately model light transport and detection in a scintillator detector.

We have previously introduced a statistics-based positioning (SBP) method to improve the positioning performance of continuous miniature crystal element (cMiCE) detectors (Joung *et al* 2002). Our initial detectors used thin crystals (e.g., 3–4 mm thick) to reduce DOI effects on performance. The SBP algorithm relies upon characterizing the light response function of each photomultiplier tube (PMT) channel versus event location (i.e., two-dimensional (x, y) event position) for positioning. Data from a focused point source are collected on a grid of X – Y positions covering the full face of the crystal. Two SBP look-up tables (LUTs) are created to characterize the detector, one LUT for the mean and one LUT for the variance of the light response function value versus (x, y) position. Each event is then positioned according to the (x, y) location that maximizes the likelihood function between the event data and the SBP LUTs.

Research efforts to allow the use of thicker crystals have led to this new method to create LUTs to characterize cMiCE detectors for DOI. Here we propose a maximum-likelihood (ML) clustering method to effectively build LUTs for different DOI regions. We first validated our method using simulated data, and then evaluated it using experimental data. The effect of using multi-DOI LUTs on intrinsic spatial resolution was also investigated.

2. Materials and methods

2.1. Data acquisition and processing

2.1.1. Simulated data. The DETECT2000 simulation package (Knoll *et al* 1988, Tsang *et al* 1995, Moisan *et al* 2000) was used to model the detector module. For this work, the crystal was modelled as a 48.8 mm \times 48.8 mm \times 8 mm slab of $\text{Lu}_2\text{SiO}_5 : \text{Ce}^{3+}$ (LSO) (index of refraction = 1.82). The two 48.8 mm \times 48.8 mm surfaces were polished. One side was directly coupled (i.e., no light guide) to the PMT with 0.5 mm of 1.44 index of refraction epoxy. The other side was backed with a diffuse reflector with a reflection coefficient (RC) of 0.98. The short sides were coated with low reflectivity paint (RC = 0.10). An 8 \times 8 array of anode pads (i.e., DETECT surfaces), 5.8 mm \times 5.8 mm with 6.08 mm centre-to-centre spacing, was placed on the backside of a 2 mm thick glass PMT window. All interactions were photoelectric (i.e., no Compton scatter). 2500 photoelectrons were produced per interaction. This accounts for the light produced by LSO and the quantum efficiency of the PMT's photocathode. The crystal was divided into 0.1 mm thick DOI slices. The number of interactions in each DOI slice was adjusted to take into account the linear attenuation coefficient of LSO. However within each 0.1 mm zone, the probability of interaction was equally distributed. A more detailed description of the simulations can be found in (Miyaka *et al* 2004).

The grid shown in figure 1 was used to characterize a region of the detector. Symmetry was used to generate the full detector LUT (i.e., 33 \times 33). The grid spacing was 1.52 mm (i.e., 1/4 the PMT anode pixel pitch distance). Each dot represents a point annihilation photon flux of 511 keV photons perpendicular to the crystal surface. A flux of 100 000 annihilation photons was used as the *training data set* to characterize the detector and a flux of 20 000 annihilation photons was used as the *testing data set* to validate our ML clustering algorithm.

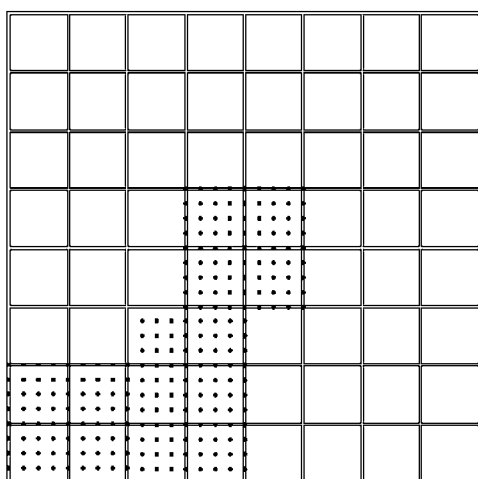


Figure 1. Grid locations (1.52 mm spacing) used to characterize the centre and corner sections of the detector for the simulated data set.

2.1.2. Experimental data. The experimental settings are the same as described in (Ling *et al* 2006). A cMiCE detector consisting of a 50 mm × 50 mm × 8 mm thick LYSO crystal (Saint Gobain, Newbury, OH) and 52 mm square, 64-channel flat panel PMT (Hamamatsu H8500, Japan) was used.

The two large area surfaces of the crystal were polished and the edges were left roughened. The roughened edges were painted black to reduce reflected light. The crystals were coupled to the PMT using Bicron BC-630 optical grease (Saint Gobain, Newbury, Ohio). The surface of the crystal opposite the PMT was painted white.

The point spot flux was produced using a 0.25 mm diameter, 23 μ Ci Na-22 source (Isotope Products, Valencia, CA) and a 2 mm × 2 mm cross-section coincidence detector placed at a distance from the source. Based upon the geometry of the setup, the point spot flux had a squarish shape and a FWHM (full width at half maximum) of \sim 0.52 mm, as illustrated in figure 2, at the front surface of the crystal. The flux broadens to \sim 0.65 mm FWHM at the rear surface of the crystal. Data were collected with the point spot fluxes normal to the detector surface on a grid with \sim 1 mm spacing in both X and Y , covering over a quarter of the crystal. 70% of the data were kept for the *training data set* with the remaining 30% used as *testing data*.

All 64 channels from the multi-anode, flat panel PMT were acquired for each coincidence event. Two 32-channel CAEN ADC cards (N792 ADCs, CAEN, Italy) were used for data acquisition. The data were acquired to an Apple computer running OS X and the Orca data acquisition software package (from CENPA, University of Washington (Howe *et al* 2004)).

Raw data were processed in the same manner as in (Ling *et al* 2006). We applied a two-step data filtering process on the raw data to preferentially select the data we used to build our SBP LUTs. In the first step, we set an energy window of \pm 20% around the photopeak to select 511 keV events that were photoelectrically absorbed in the crystal, as shown in figure 3. Second, we used an ‘Anger mask’ technique to reduce the number of Compton scattered events that were used for characterizing the detector. Events within the photopeak energy window were positioned using Anger logic. A contour mask at 20% of the maximum height as illustrated in figure 4 was applied. Events within the mask are more likely single

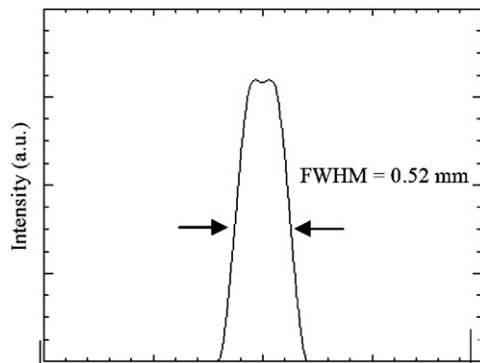


Figure 2. Profile of the point spot flux used in the experiment. From the geometry of the experimental setup, the point spot flux has a FWHM of 0.52 mm.

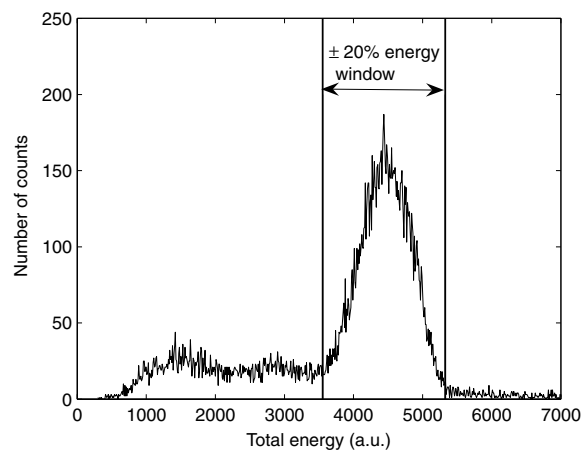


Figure 3. Energy window of $\pm 20\%$ around the photopeak.

photoelectric absorption events and are kept for LUT building. By using an ‘Anger mask’, we are able to eliminate many of the Compton scattered events from biasing the true relationship between the photon interaction location and the light distribution. The ‘Anger mask’ technique is further described in section 2.1.3 *Anger mask validation*.

Because of its stochastic nature, it is not possible to obtain a testing data set with known spatial position (x , y) and DOI for each event at the same time. Most DOI calibration processes use an incident photon flux on the side of the crystal, which offers relatively good control over DOI. However because of the dimensions of our crystal, this methodology would only allow us to test a small fraction of the crystal along its edge and not the centre section of the detector.

Therefore, for testing we adjusted the point photon flux to a 45° incidence angle relative to the crystal surface along the X -axis, as shown in figure 5. Thus ideally DOI can be referenced by the x coordinate of the positioned event. An advantage of this acquisition scheme is that we can obtain testing data sets at any section of the crystal. A second set of testing data to evaluate our DOI method was collected on the same quarter of the crystal as the training data. Data were collected on a 10×10 grid with ~ 1 mm spacing in both axes in the centre and

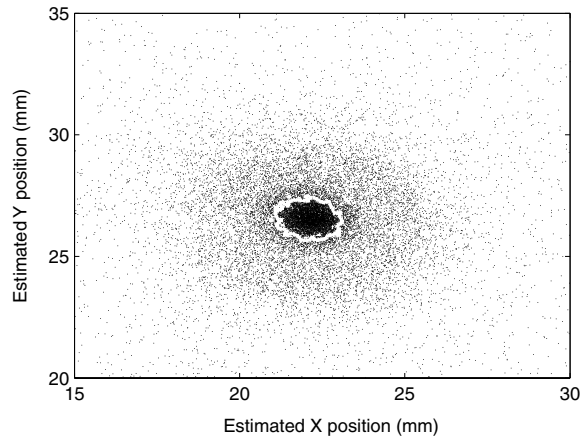


Figure 4. Point source using Anger positioning. Only points within the light Anger mask circle are used for SBP look-up table generation.

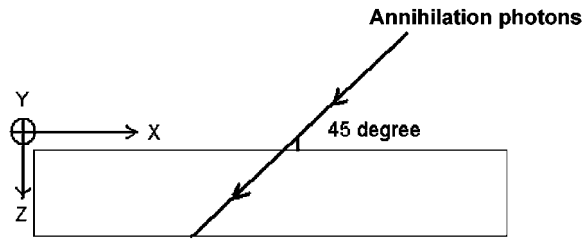


Figure 5. An annihilation photon beam incident at 45° relative to the surface. The depth of the first photon interaction in the crystal is equal to the spatial position along the X-axis.

corner regions of the detector. Energy windowing as described above was also applied to the data. No ‘Anger masking’ is applied to the testing data sets.

2.1.3. Anger mask validation. Data from the DETECT simulations were used to generate the empirical light propagation probability function $p_i(x, y, z)$, which is the probability of an isotropically outgoing light photon from location (x, y, z) inside the crystal reaching the i th PMT channel. GEANT was used to simulate the photoelectric absorption and Compton scattering of 10 000 perpendicularly incident annihilation photons at each characterization position as shown in figure 1. We assumed a LSO light yield N of 23 000 scintillation photons/MeV and a PMT efficiency Q of 22.5% (Moisan *et al* 1997). Non-proportional scintillation was also implemented by discounting the number of light photons at each interaction vertex. The correction factor R was taken from the experimental electron response function from (Rooney *et al* 1997). For each event the expected number of light photons received by the i th PMT channel, λ_i can be calculated by

$$\lambda_i = \sum_j N Q p_i(\vec{x}_j) R(E_j) E_j, \quad (1)$$

where j is the index for interaction vertex, and E_j is the energy deposited at the j th interaction vertex. N , Q , p_i and R are as described above. We further assume that the response of each

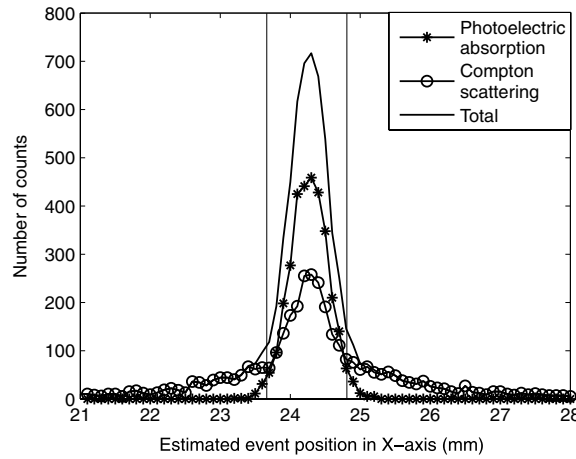


Figure 6. Effect of Anger mask on removing scattered events. The Anger mask using a 20% contour, shown as two solid lines in the plot, can effectively exclude large angle Compton scattered events, while including most of the single interaction photoelectric events.

channel follows an independent Poisson process with λ_i . Thus a new set of simulated data with the effect of Compton scattering was generated.

A sample projection of an Anger positioning result is shown in figure 6. Projections of single interaction photoelectric absorption events and Compton scatter events are also shown. The two solid lines show the Anger mask using the contour at 20% of the maximum. Events outside the mask were filtered out. At the cost of excluding a small portion of the single interaction photoelectric absorption events, a good percentage of the Compton scatter events, especially those with large angle Compton scatter, were excluded. The results support the Anger mask technique and that the height of the contour is appropriate.

2.2. Statistics-based (maximum-likelihood) positioning algorithm

Suppose, the distributions of observing PMT outputs $M = M_1, M_2, \dots, M_n$ for scintillation position \vec{x} , are independent normal distributions with mean $\mu_i(\vec{x})$ and standard deviation $\sigma_i(\vec{x})$.

The likelihood function for making any single observation m_i from distribution M_i given \vec{x} is

$$L[\vec{x}|(m_1, m_2, \dots, m_n)] = \prod_{i=1}^n \frac{1}{\sqrt{2\pi}\sigma_i(\vec{x})} \exp\left[-\frac{(m_i - \mu_i(\vec{x}))^2}{2\sigma_i^2(\vec{x})}\right]. \quad (2)$$

The log-likelihood function reduces to

$$\ln L = -\sum_{i=1}^n \left[\frac{(m_i - \mu_i(\vec{x}))^2}{2\sigma_i^2(\vec{x})} + \ln \sigma_i(\vec{x}) \right] + \text{const}. \quad (3)$$

Finally, the ML estimator of event position is given by

$$\hat{\vec{x}} = \arg \min_{\forall \vec{x}, \vec{x}=\hat{\vec{x}}} \sum_{i=1}^n \left[\frac{(m_i - \mu_i(\vec{x}))^2}{2\sigma_i^2(\vec{x})} + \ln \sigma_i(\vec{x}) \right]. \quad (4)$$

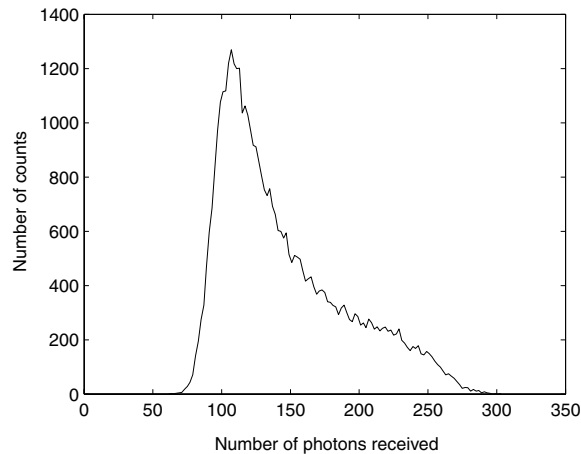


Figure 7. Sample light collection histogram for a single PMT channel from simulated data, illustrating non-Gaussian characteristics. For photon fluxes directly over one of the PMT's anodes the amount of light collected by that anode (channel) varies significantly with DOI. The non-exponential shape of the high-end tail is a result of the depth-dependent light collection efficiency for the PMT channel.

2.3. Look-up table generation

It is obvious that the essential components of the SBP algorithm are $\mu_i(\vec{x})$ and $\sigma_i(\vec{x})$. If μ and σ are functions of $\vec{x} = (x, y)$, the SBP method will give an estimate of the 2D spatial position. If the functions are of $\vec{x} = (x, y, z)$, the interaction position can be estimated in 3D simultaneously. Since it is impossible to derive closed form functions, the functions were determined from the simulated and experimental training data sets.

A sample light collection histogram for a single PMT channel at one of the characterization locations from the simulated data set is illustrated in figure 7. It is the histogram of the amount of light received by the PMT channel underneath the point spot flux. The skewness of the distribution is caused by the depth-dependent light collection efficiency of the PMT channel. Only data after energy windowing and applying the 'Anger mask' were used. Depending upon the location of the point flux, the histograms may vary in the amount of light received and the skewness of the distribution. The mean and standard deviation of the light response are calculated for each PMT channel at each characterization spot.

LUTs representing the mean and standard deviation of the detector response function (DRF) for each PMT channel versus grid position were generated from the individual light collection histograms. For the simulated data set, the initial tables were $33 \times 33 \times 64$, where 33×33 is the number of grid positions and 64 is the number of PMT channels. Simulations were not run for each grid position. Instead symmetry of the detector was used to generate the full LUTs. Cubic spline interpolation was then used to expand the LUTs to 129×129 (or 0.38 mm sampling) $\times 64$. The LUTs were used with the SBP algorithm to estimate the location and DOI of the detected event.

Similar LUTs were built using the experimental training data. The difference is that the LUTs covered just over a quarter of the detector and the sample spacing was ~ 0.2 mm after interpolation. Unlike the simulation, full LUTs covering the whole detector surface were not built.

Two sets of LUTs were generated for both the simulated and experimental data sets. The first set of LUTs, or 2D LUTs, was for the mean and standard deviation of the PMT signals

using the filtered training data at each grid position, which depends only on the X and Y position. For the second set of tables, the data were first divided into two or four DOI regions by the ML clustering method discussed below. For each of the DOI regions, LUTs of mean and standard deviation were calculated and then combined into multi-DOI LUTs.

2.4. Maximum-likelihood clustering algorithm

Our ML clustering algorithm utilizes the fact that the light distribution pattern varies continuously and smoothly with DOI so scintillation events happening in similar DOI regions of the crystal will produce similar light distribution patterns. Our method clusters the events based on the similarity in the empirically measured light distribution patterns, instead of modelling the distribution.

The major steps of the ML clustering algorithm are described below.

Step 1. For the filtered training data at each position, find the PMT channel N receiving the maximum amount of light. Separate the data into two initial groups, as illustrated by the solid line in figure 8(a). Group 1 is events with pulse height in channel N less than the median. Group 2 is events with pulse height in N greater than the median.

Step 2. For each of the sets of data (i.e., groups 1 and 2) generate the mean $\mu_i^{(j)}$ and standard deviation $\sigma_i^{(j)}$, where i is the number of the PMT channel and j is the group number.

Step 3. For each event calculate the likelihood ratio (LR) between groups 1 and 2:

$$\text{LR} = \frac{L[\text{Group 1} | (m_1, m_2, \dots, m_n)]}{L[\text{Group 2} | (m_1, m_2, \dots, m_n)]}. \quad (5)$$

Separation in LR can be used to tune the number of events falling in each group. Here we choose the separation value to be 1. After all the data has been sorted go back to step 2 and iterate.

Step 4. After a stable separation is reached, the final mean and standard deviation are generated where they represent the light response LUTs for groups 1 and 2, respectively. The testing data sets will be used to validate that the two groups correspond to front (close to entrance surface) and back (close to PMT) DOI regions of the detector.

The idea behind the initial grouping in step 1 is that the signal from channel N correlates with interaction depth, as interactions near the photocathode will have a large amount of light in this channel and a smaller fraction of the light will shine on this channel when the interaction is farther away.

In step 3, we proposed to set the separation at $\text{LR} = 1$, which does not force an equal number of events to be assigned to groups 1 and 2. Instead we believe that a ‘natural’ separation will be more powerful in differentiating the future testing events than a ‘forced’ separation when the fraction of events assigned to each depth is predetermined.

DOI ranges corresponding to different DOI regions were calculated from the number of events clustered in each group. For two DOI regions, the two regions are separated at a depth of 4.24 mm. The DOI region of $[0, 4.24 \text{ mm}]$ will be referred to as *front*; $[4.24 \text{ mm}, 8 \text{ mm}]$ region will be referred to as *back*. For four DOI regions, the separation depths are 1.95 mm, 3.95 mm and 5.93 mm.

For the algorithm as described we are only dividing the detector into two DOI regions for the experimental data. In principle the detector can be divided into more DOI regions, where the maximum number will mainly be limited by the statistics of the data used to characterize the detector.

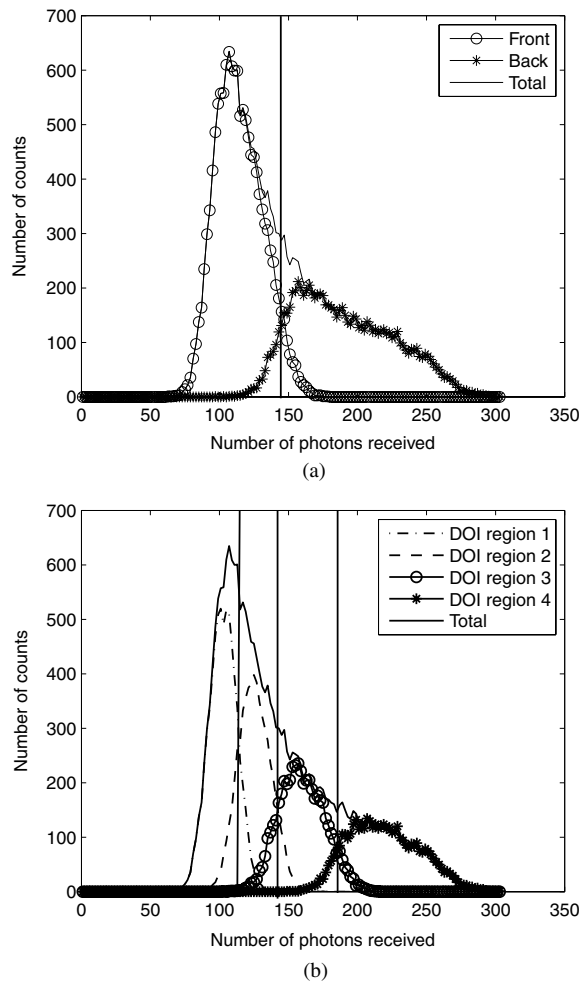


Figure 8. Sample light collection function after clustering from the simulated data set (a) two DOI regions clustering result, (b) four DOI regions clustering result. The solid lines in the plots illustrate the initial guess of the DOI groupings. Depending upon the location of the photon flux on the crystal face, the amount of overlap can be greater or less than shown.

3. Results

3.1. Method validation using simulated data

The ML clustering algorithm was first validated using the DETECT2000 simulated data. The training data set was separated into two and four DOI regions. A sample light collection histogram after ML clustering is shown in figure 8. 2D and multi-DOI LUTs are also shown in figure 9. The characteristics of the multi-DOI LUTs for different DOI were as we expected. The LUT for events interacting near the PMT is more localized; the light distribution for events interacting near the entrance surface of the crystal is more spread out.

The DOI results from the SBP method were examined against the true DOI from simulation. *Misclassification rates*, defined as the number of misclassified events divided by the total number of events, were calculated for each testing data set.

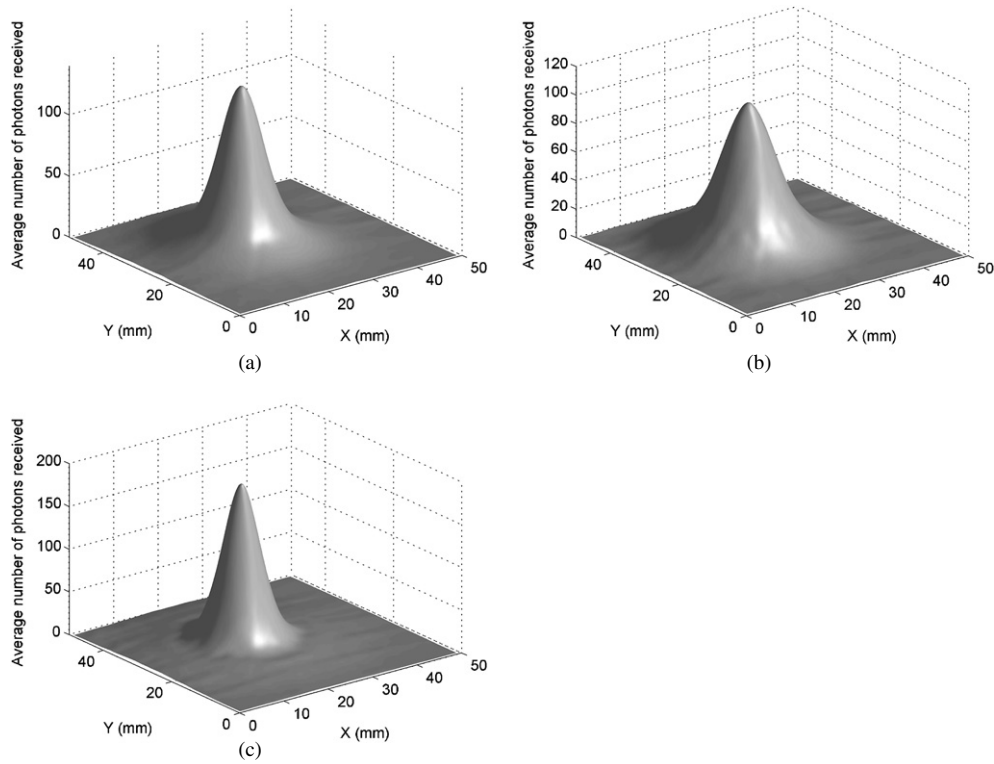


Figure 9. Sample 2D and 2-DOI 3D LUTs from simulated data: (a) the mean LUT for a given channel; (b), (c) mean LUT of front (b) and back (c) DOI regions.

Table 1. Misclassification rate for simulated data.

LUT used	Misclassification rate (%)	
	Centre	Corner
Two DOI regions	3.5 ± 0.5	4.6 ± 1.0
Four DOI regions	10.2 ± 0.7	13.9 ± 4.6

The sample averages of the estimated DOI using the multi-DOI LUTs versus the true DOI from simulation were plotted in figure 10. Different DOI regions determined previously were separated by solid lines in the graphs. Results are summarized in table 1. For 2-depths, the misclassification rate is 3.5% for points in the centre section of the detector and 4.6% for the corner section. For 4-depths, the misclassification rates are 10.2% and 13.9% for the centre and corner sections, respectively. The results show that the ML clustering method can effectively cluster events into four DOI groups according to the similarity of their light distribution pattern.

3.2. Performance evaluation using experimental data

An experimental light collection histogram after ML clustering is shown in figure 11.

The 45° incident angle experimental testing data were positioned using SBP with multi-DOI LUTs derived from the cMiCE training data set. DOI results were examined using the

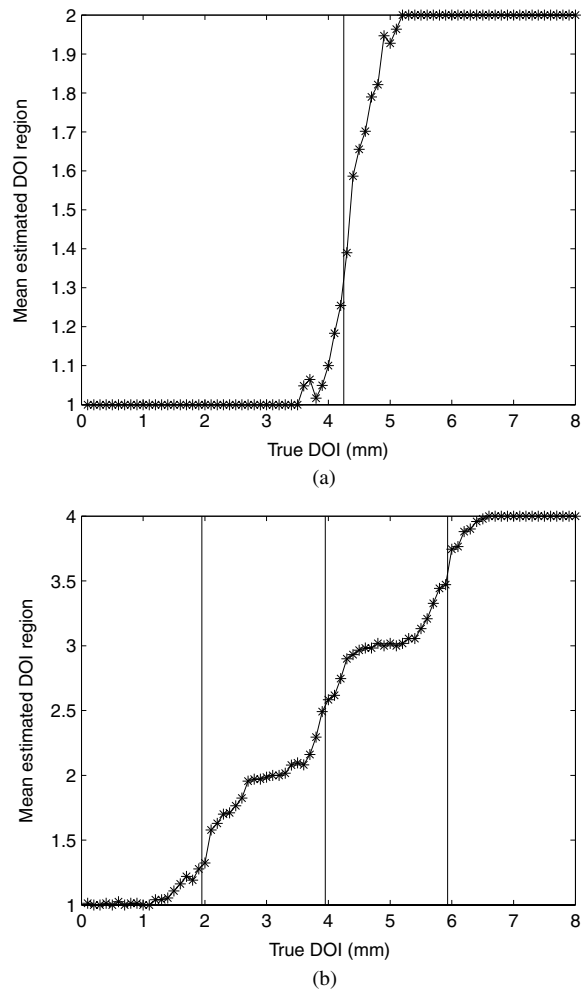


Figure 10. DOI results of the simulated data set using (a) 2-DOI and (b) 4-DOI LUTs. The horizontal axis is the true DOI from simulation; the vertical axis is the average of the estimated DOI for all points at each depth.

estimated spatial positions. Since the flux is incident at a 45° angle to the surface of the crystal along the X -axis, we would expect that all events should have the same Y position, whereas they should be spread out along the X -axis, as illustrated in figures 12 and 13. The region of interaction was determined as the 8 mm interval with the most number of events, shown as the section between the two solid lines in figure 12. Events outside the interaction region were excluded from further investigation. An enlarged view of the interaction region is shown in figure 14. The top graph in figure 14 is the average DOI region number for each estimated X position. Since group 1 corresponds to the front and group 2 corresponds to the back, figure 14 correctly illustrates the gradual change of depth with position with respect to the X -axis. DOI results from three adjacent flux positions with ~ 1 mm spacing are illustrated in figure 15.

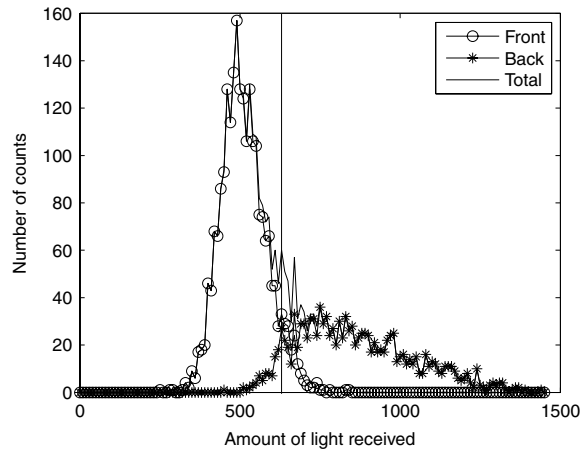


Figure 11. Sample light collection histogram after clustering from the experimental data. The solid line represents the initial guess for the separation of the DOI groups.

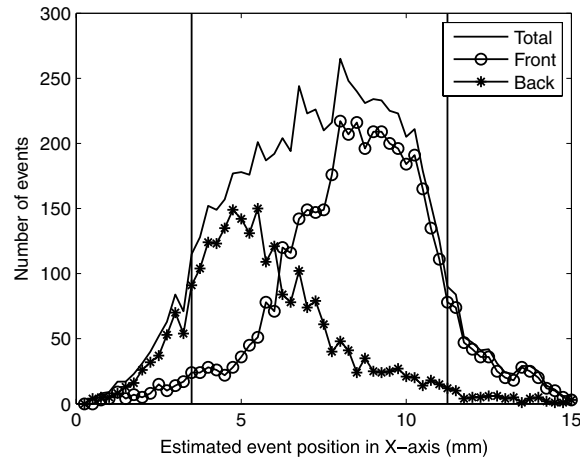


Figure 12. SBP results with 2-DOI LUT projected to the X-axis. The events in the front region are mainly on the right side; events in the back region are on the left side. This result is consistent with the experimental setup.

The calculated MRs (misclassification rates) for the experimental data are higher than those for the simulated data. The estimated X position was used as the true DOI. For example, in figure 14, all events with X position between 7.74 mm and 11.5 mm are considered events happening in the front layer; those between 3.5 mm and 7.74 mm are considered in the back layer. Misclassified events are those that are assigned to the wrong group. The average MR for the centre section of the detector was $24.7 \pm 2.1\%$. Note that this estimate is not adjusted for the intrinsic spatial resolution of the detector and therefore is an upper bound on the misclassification rate.

There are a number of factors that can contribute to the MR. The three main ones are discussed. The first is the size of source. Since the source has a finite size of 0.52 mm in

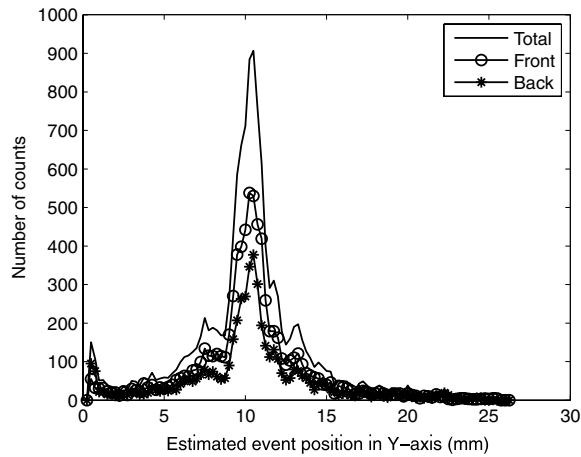


Figure 13. SBP results with 2-DOI LUT projected to Y -axis. As expected the estimated Y positions for both the front and back group are the same.

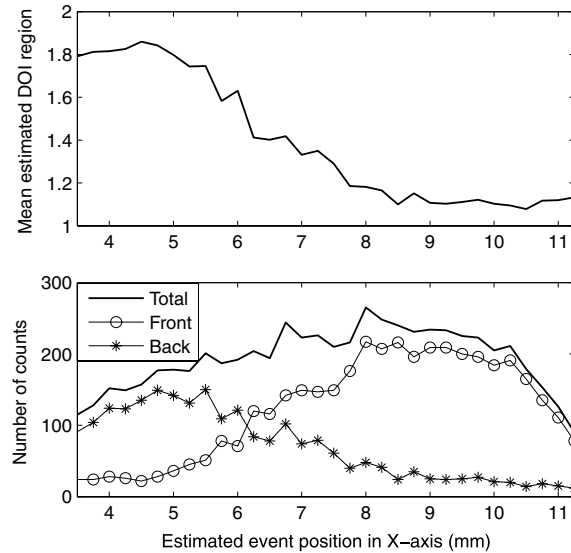


Figure 14. Top: $E[D\hat{O}I|\hat{X}]$ versus \hat{X} ; Bottom: enlarged view of the interaction region (region between solid lines in figure 12).

diameter, at any X position, the DOI can be off by up to ~ 0.7 mm. The second is uncertainty in the spatial positioning. The intrinsic spatial resolution limits the accuracy of our depth estimate. The third is Compton scattering. Multi-interaction events falling within the energy window can lead to incorrect DOI estimation. This is a limitation of almost all DOI detector implementations.

The first testing data set, i.e., the perpendicularly incident data, was positioned using both the 2D LUT and the 2-DOI LUT. As shown in table 2, the intrinsic spatial resolution at

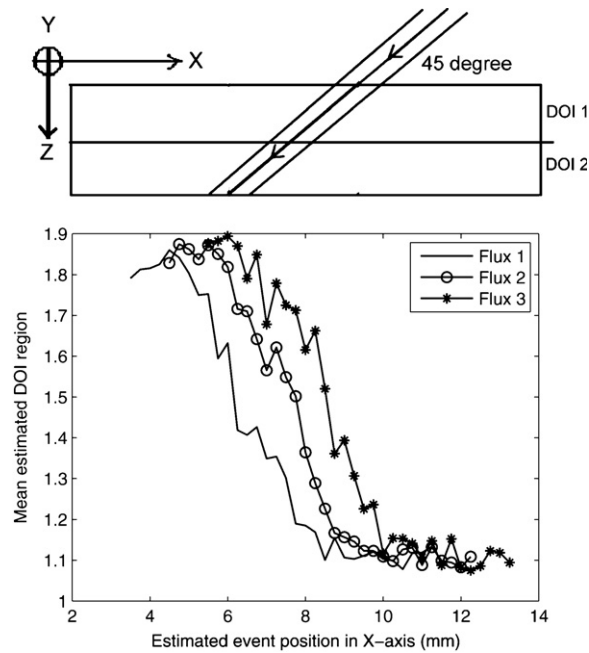


Figure 15. Overlay of three $E[\hat{DOI}|\hat{X}]$ versus \hat{X} curves. Point flux was stepped in ~ 1 mm increments along the X -axis. Except for the statistical noise, the results are consistent with each other.

Table 2. Intrinsic resolution results.

LUT used	Resolution in X (mm)		Resolution in Y (mm)	
	Centre	Corner	Centre	Corner
2D LUT	1.30 ± 0.16	2.3 ± 0.5	1.35 ± 0.13	2.4 ± 0.6
2-DOI LUT	1.27 ± 0.11	1.60 ± 0.38	1.30 ± 0.09	1.79 ± 0.58

the centre section was maintained, while significant improvement was observed at the corner section of the detector.

4. Summary and conclusion

Our ML clustering method proved to be a consistent and reliable way to generate DOI LUTs, thus making it possible to characterize the 3D LRF of our cMiCE detector. High spatial resolution is maintained in the centre and is improved near the edge of the detector, while extracting DOI information. The SBP algorithm uses the mean and variance to characterize the LRF. The model assumes a normal distribution for the light probability density functions. After clustering, the approximation of the normal distribution is better met. This is the main reason for the improvement of spatial resolution, especially in the area near the edge of the crystal.

A strength of this method is that no extra treatments to the standard cMiCE crystal or measurements are needed. Thus it is simple to implement. Another feature of this method

is that it is coherent with the SBP algorithm. DOI and spatial positions can be estimated simultaneously.

Since we do not consider other sources of noise in the detector system, such as the noise from the PMT, the misclassification rate by our algorithm will be greater than the simulation result. For our experimental results, the main reason for misclassification of events is Compton scattering. It is also the main reason the misclassification rate is so different between our simulated and experimental results. From our experimental results (i.e., figure 14), misclassification due to Compton scatter is 15–20%. In the transition region additional sources of error are the size of source, uncertainty in estimating X position, and intrinsic error from the algorithm.

Being able to extract depth of interaction from PET detectors can have a tremendous impact on future PET detector designs. For commercial, human PET systems, detectors that provide some DOI information will allow systems to be built with smaller ring diameters. Having a smaller ring diameter will translate into lower cost scanners or scanners with a longer axial field of view. A scanner with a longer axial field of view can shorten imaging times for patient studies. For specialty PET systems that require ultrahigh spatial resolution (e.g., <2 mm FWHM) detectors that provide some DOI information can lead to scanners with much higher detection efficiency. This is especially important for small animal imaging systems where the injected dose may be significantly limited by the specific activity of the labelled compound (e.g., for receptor imaging studies).

We will further examine the performance of the ML clustering method on even thicker cMiCE detectors. We will also evaluate the impact of DOI capability on the performance of a small animal PET scanner using cMiCE detectors through simulation and experiment. Furthermore, the effect of Compton scattering and other factors on misclassification rate will be studied through simulation.

Acknowledgments

This work was supported in part by NIH-NIBIB grants: R21/R33 EB001563 and R01 EB002117.

References

- Burr K C *et al* 2004 Evaluation of a prototype small animal PET detector with depth-of-interaction encoding *IEEE Trans. Nucl. Sci.* **51** 1791–8
- Howe M A *et al* 2004 Sudbury neutrino observatory neutral current detector acquisition software overview *IEEE Trans. Nucl. Sci.* **51** 878–83
- Joung J, Miyaoka R S and Lewellen T K 2002 CMiCE: a high resolution animal PET using continuous LSO with a statistics based positioning scheme *Nucl. Instrum. Methods A* **489** 584–98
- Knoll G F *et al* 1988 Light collection scintillation detector composited for neutron detection *IEEE Trans. Nucl. Sci.* **35** 872–5
- LeBlanc J W and Thompson R A 2004 A novel PET detector block with three dimensional hit position encoding *IEEE Trans. Nucl. Sci.* **51** 746–51
- Lerche C W *et al* 2005 Depth of gamma-ray interaction within continuous crystals from the width of its scintillation light-distribution *IEEE Trans. Nucl. Sci.* **52** 560–72
- Ling T *et al* 2006 Performance comparisons of continuous miniature crystal element detectors *IEEE Tran. Nucl. Sci.* **53** 2513–8
- Miyaoka R S and Lee K 2004 Investigation of detector light response modeling for a thick continuous slab detector *IEEE Nucl. Sci. Symp. Conf. Rec. (Rome)* **4** 2479–82
- Miyaoka R S *et al* 1998 Design of a depth of interaction (DOI) PET detector module *IEEE Trans. Nucl. Sci.* **45** 1069–73
- Moisan C *et al* 2000 *DETECT2000 Version 5.0*

- Moisan C *et al* 1997 Simulating the performance of an LSO based position encoding detector for PET *IEEE Trans. Nucl. Sci.* **44** 2450–8
- Moses W W *et al* 1993 Performance of a PET detector module utilizing an array of silicon photodiodes to identify the crystal of interaction *IEEE Trans. Nucl. Sci.* **40** 1036–40
- Rooney B D and Valentine J D 1997 Scintillation light yield nonproportionality: calculating photon response using measured electron response *IEEE Trans. Nucl. Sci.* **44** 509–16
- Saoudi A *et al* 1999 Investigation of depth-of-interaction by pulse shape discrimination in multicrystal detectors read out by avalanche photodiodes *IEEE Trans. Nucl. Sci.* **46** 462–7
- Seidel J *et al* 1998 Depth identification accuracy of a three layer phoswich PET detector module *IEEE Trans. Nucl. Sci.* **46** 485–90
- Shao Y *et al* 2002 Dual APD array readout of LSO crystals: optimization of crystal surface treatment *IEEE Trans. Nucl. Sci.* **49** 649–54
- Tavernier S *et al* 2005 A high-resolution PET detector based on continuous scintillators *Nucl. Instrum. Methods A* **537** 321–5
- Tsang G *et al* 1995 A simulation to model position encoding multi-crystal PET detectors *IEEE Trans. Nucl. Sci.* **42** 2236–43
- Yamamoto S and Ishibashi H 1998 A GSO depth of interaction detector for PET *IEEE Trans. Nucl. Sci.* **45** 1078–82